

We are IntechOpen, the world's leading publisher of Open Access books Built by scientists, for scientists

6,900

Open access books available

186,000

International authors and editors

200M

Downloads

Our authors are among the

154

Countries delivered to

TOP 1%

most cited scientists

12.2%

Contributors from top 500 universities



WEB OF SCIENCE™

Selection of our books indexed in the Book Citation Index
in Web of Science™ Core Collection (BKCI)

Interested in publishing with us?
Contact book.department@intechopen.com

Numbers displayed above are based on latest data collected.
For more information visit www.intechopen.com



Electronic Structures of Tetragonal ABX_3 : Role of the B-X Coulomb Repulsions for Ferroelectricity and Piezoelectricity

Kaoru Miura and Hiroshi Funakubo

Additional information is available at the end of the chapter

<http://dx.doi.org/10.5772/52187>

1. Introduction

Since Cohen proposed an origin for ferroelectricity in perovskites (ABX_3) [1], investigations of ferroelectric materials using first-principles calculations have been extensively studied [2-20]. Currently, using the pseudopotential (PP) methods, most of the crystal structures in ferroelectric ABX_3 can be precisely predicted. However, even in $BaTiO_3$, which is a well-known ferroelectric perovskite oxide with tetragonal structure at room temperature, the optimized structure by the PP methods is strongly dependent on the choice of the Ti PPs as illustrated in Fig. 1; preparation for Ti 3s and 3p semicore states in addition to Ti 3d, 4s, and 4p valence states is essential to the appearance of the tetragonal structure. This is an important problem for ferroelectricity, but it has been generally recognized for a long time that this problem is within an empirical framework of the calculational techniques [21].

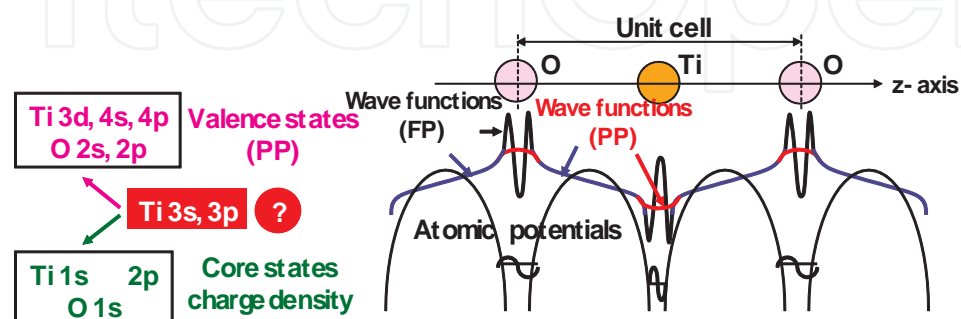


Figure 1. Illustration of the choice of Ti 3s and 3p states in pseudopotentials.

It is known that ferroelectric state appears when the long-range forces due to the dipole-dipole interaction overcome the short-range forces due to the Coulomb repulsions. Investigations about the relationship between the Ti-O Coulomb repulsions and the appearance of ferroelectricity in $ATiO_3$ ($A = Ba, Pb$) were reported both theoretically and experimentally. Theoretically, Cohen first proposed the hybridization between Ti 3d state and O 2p state (Ti 3d-O 2p) as an origin for ferroelectricity in $BaTiO_3$ and $PbTiO_3$ [1]. On the other hand, we investigated [20] the influence of the Ti- O_z Coulomb repulsions on Ti ion displacement in tetragonal $BaTiO_3$ and $PbTiO_3$, where O_z denotes the O atom to the z-axis (Ti is displaced to the z-axis). Whereas the hybridization between Ti 3d state and O_z 2p_z state stabilize Ti ion displacement, the strong Coulomb repulsions between Ti 3s and 3p_z states and O 2p_z states do not favourably cause Ti ion displacement. Experimentally, on the other hand, Kuroiwa *et al.* [22] showed that the appearance of ferroelectric state is closely related to the total charge density of Ti-O bonding in $BaTiO_3$. As discussed above, investigation about a role of Ti 3s and 3p states is important in the appearance of the ferroelectric state in tetragonal $BaTiO_3$, in addition to the Ti 3d-O 2p hybridization as an origin of ferroelectricity [1].

It seems that the strong B - X Coulomb repulsions affect the most stable structure of ABX_3 . It has been well known that the most stable structure of ABX_3 is closely related to the tolerance factor t ,

$$t = \frac{r_A + r_X}{\sqrt{2} (r_B + r_X)}, \quad (1)$$

where r_A , r_B , and r_X denote the ionic radii of A , B , and X ions, respectively [23]. In general ferroelectric ABX_3 , the most stable structure is tetragonal for $t \gtrsim 1$, cubic for $t \approx 1$, and rhombohedral or orthorhombic for $t \lesssim 1$. In fact, $BaTiO_3$ with $t = 1.062$ shows tetragonal structure in room temperature. However, recently, $BiZn_{0.5}Ti_{0.5}O_3$ (BZT) with $t = 0.935$ was experimentally reported [24] to show a tetragonal $PbTiO_3$ -type structure with high c/a ratio (1.211). This result is in contrast to that of $BiZn_{0.5}Mg_{0.5}O_3$ (BMT) with $t = 0.939$, *i.e.*, the most stable structure was reported to be the orthorhombic or rhombohedral structure [25, 26]. Several theoretical papers of BZT have been reported [4-6], but the role of the Zn-O Coulomb repulsions in the appearance of the tetragonal structure has not been discussed sufficiently.

Piezoelectric properties in ABX_3 are also closely related to the crystal structure. Investigations of the relationship between piezoelectric properties and the crystal structure of ABX_3 by first-principles calculations have been extensively studied [2-19]. Moreover, phenomenological investigations of the piezoelectric properties have been also performed [27, 28]. However, it seems that the piezoelectric properties in the atomic level have not been sufficiently investigated. Therefore, further theoretical investigation of the relationship between piezoelectric properties and the crystal structure of ABX_3 , especially the B - X Coulomb repulsions, should be needed.

Recently, we investigated the roles of the Ti-O Coulomb repulsions in the appearance of a ferroelectric state in tetragonal $BaTiO_3$ by the analysis of a first-principles PP method [11-15]. We investigated the structural properties of tetragonal and rhombohedral $BaTiO_3$ with two kinds of Ti PPs, and propose the role of Ti 3s and 3p states for ferroelectricity. We also inves-

tingated the role of the Zn-O Coulomb repulsions in the appearance of a ferroelectric state in tetragonal BZT [10, 13]. Moreover, we also investigated the structural, ferroelectric, and piezoelectric properties of tetragonal ABX₃ and discussed the piezoelectric mechanisms based on the B-X Coulomb repulsions [12, 14, 15, 18, 19].

In this chapter, based on our recent papers and patents [10-19], we discuss a general role of B-X Coulomb repulsions for the appearance of the ferroelectric state in ABX₃. Then, we also discuss the relationship between the B-X Coulomb repulsions and the piezoelectric properties of tetragonal ABX₃.

2. Methodology

The calculations for ABX₃ were performed using the ABINIT code [29], which is one of the norm-conserving PP (NCP) methods. Electron-electron interaction was treated in the local-density approximation (LDA) [30]. Pseudopotentials were generated using the OPIUM code [31]:

- i. In BaTiO₃, 5s, 5p and 6s electrons for Ba PP, and 2s and 2p electrons for O PP were treated as semicore or valence electrons, respectively. Moreover, in order to investigate the role of Ti 3s and 3p states, two kinds of Ti PPs were prepared: the Ti PP with 3s, 3p, 3d and 4s electrons treated as semicore or valence electrons (Ti3spd4s PP), and that with only 3d and 4s electrons treated as valence electrons (Ti3d4s PP). In both PPs, the differences between the calculated result and experimental one are within 1.5 % of the lattice constant and within 10 % of the bulk modulus in the optimized calculation of bulk Ti. The cutoff energy for plane-wave basis functions was set to be 50 Hartree (Hr). The number of atoms in the unit cell was set to be five, and a 6×6×6 Monkhorst-Pack *k*-point mesh was set in the Brillouin zone of the unit cell. Positions of all the atoms were optimized within the framework of the tetragonal (*P4mm*) or rhombohedral (*R3m*) structure.
- ii. In BZT and BMT, 5d, 6s, and 6p electrons for Bi PP, and 2s and 2p electrons for O PP were treated as semicore or valence electrons, respectively. Moreover, in order to investigate the roles of Zn and Ti 3s and 3p states, and Mg 2s and 2p states, two types of PPs were prepared: the PPs with only Zn and Ti 3d and 4s states, and Mg 3s states, considered as valence electrons (Case I), Zn and Ti 3s, 3p, 3d, and 4s states, and Mg 2s, 2p, and 3s states considered as semicore or valence electrons (Case II). The cutoff energy for plane-wave basis functions was set to be 70 Hr for Case I and 110 Hr for Case II. A 4×4×4 Monkhorst-Pack *k*-point mesh was set in the Brillouin zone of the unit cell. The calculated results can be discussed within 0.02 eV per formula unit (f.u.) using the above conditions. The present calculations were performed for the monoclinic, rhombohedral, and A-, C-, and G-type tetragonal structures. The number of atoms in the unit cell was set to be 10 for the rhombohedral and monoclinic structures, and 20 for the A-, C-, and G-type tetragonal structures. Positions of all the atoms were optimized within the framework of the rhombohedral (*R3*), monoclinic (*Pm*), and tetragonal (*P4mm*) structures.

- iii. Relationship between the B - X Coulomb repulsions and the piezoelectric properties in tetragonal ABX_3 is investigated. The pseudopotentials were generated using the opium code [31] with semicore and valence electrons (e.g., Ti3spd4s PP), and the virtual crystal approximation [32] were applied to several ABX_3 .

Spontaneous polarizations and piezoelectric constants were also evaluated, due to the Born effective charges [33]. The spontaneous polarization of tetragonal structures along the [001] axis, P_3 , is defined as

$$P_3 = \sum_k \frac{ec}{\Omega} Z_{33}^*(k) u_3(k), \quad (2)$$

where e , c , and Ω denote the charge unit, lattice parameter of the unit cell along the [001] axis, and the volume of the unit cell, respectively. $u_3(k)$ denotes the displacement along the [001] axis of the k th atom, and $Z_{33}^*(k)$ denotes the Born effective charges [33] which contributes to the P_3 from the $u_3(k)$.

The piezoelectric e_{33} constant is defined as

$$e_{3j} = \left(\frac{\partial P_3}{\partial \eta_j} \right)_u + \sum_k \frac{ec}{\Omega} Z_{33}^*(k) \frac{\partial u_3(k)}{\partial \eta_j} \quad (j = 3, 1), \quad (3)$$

where e and Ω denote the charge unit and the volume of the unit cell. P_3 and c denote the spontaneous polarization of tetragonal structures and the lattice parameter of the unit cell along the [001] axis, respectively. $u_3(k)$ denotes the displacement along the [001] axis of the k th atom, and $Z_{33}^*(k)$ denotes the Born effective charges which contributes to the P_3 from the $u_3(k)$. η_3 denotes the strain of lattice along the [001] axis, which is defined as $\eta_3 \equiv (c - c_0)/c_0$; c_0 denotes the c lattice parameter with fully optimized structure. On the other hand, η_1 denotes the strain of lattice along the [100] axis, which is defined as $\eta_1 \equiv (a - a_0)/a_0$; a_0 denotes the a lattice parameter with fully optimized structure. The first term of the right hand in Eq. (3) denotes the clamped term evaluated at vanishing internal strain, and the second term denotes the relaxed term that is due to the relative displacements.

The relationship between the piezoelectric d_{33} constant and the e_{33} one is

$$d_{33} \equiv \sum_{j=1}^6 s_{3j}^E \times^T (e_{3j}), \quad (4)$$

where s_{3j}^E denotes the elastic compliance, and `` T '' denotes the transposition of matrix elements. The suffix j denotes the direction-indexes of the axis, *i.e.*, 1 along the [100] axis, 2 along the [010] axis, 3 along the [001] axis, and 4 to 6 along the shear directions, respectively.

3. Results and discussion

3.1. Ferroelectricity

3.1.1. Role of Ti 3s and 3p states in ferroelectric BaTiO₃

Figures 2(a) and 2(b) show the optimized results for the ratio c/a of the lattice parameters and the value of the Ti ion displacement (δ_{Ti}) as a function of the a lattice parameter in tetragonal BaTiO₃, respectively. Results with arrows are the fully optimized results, and the others results are those with the c lattice parameters and all the inner coordination optimized for fixed a . Note that the fully optimized structure of BaTiO₃ is tetragonal with the Ti3spd4s PP, whereas it is cubic with the Ti3d4s PP. This result suggests that the explicit treatment of Ti 3s and 3p semicore states is essential to the appearance of ferroelectric states in BaTiO₃.

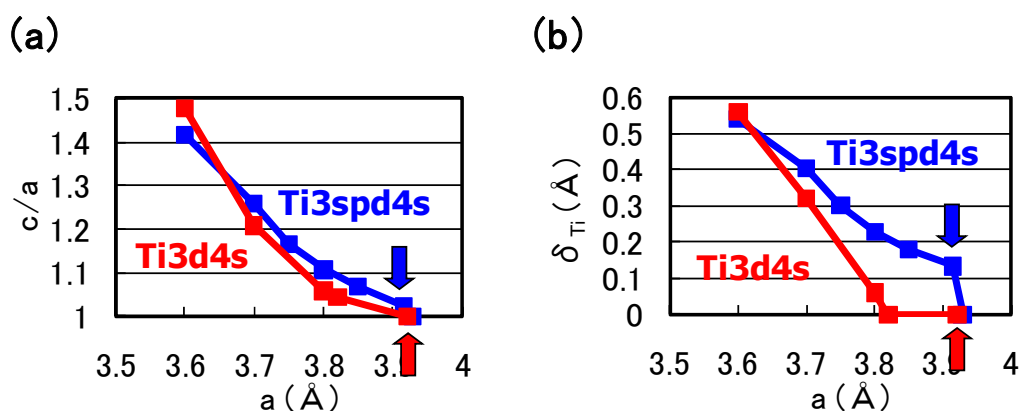


Figure 2. Optimized calculated results in tetragonal BaTiO₃. Results with arrows are the fully optimized results [11].

The calculated results shown in Fig. 2 suggest that the explicit treatment of Ti 3s and 3p semicore states is essential to the appearance of ferroelectric states in BaTiO₃. In the following, we investigate the role of Ti 3s and 3p states for ferroelectricity from two viewpoints.

One viewpoint concerns hybridizations between Ti 3s and 3p states and other states. Figure 3(a) and 3(b) shows the total density of states (DOS) of tetragonal BaTiO₃ with two Ti PPs. Both results are in good agreement with previous calculated results [7] by the full-potential linear augmented plane wave (FLAPW) method. In the DOS with the Ti3spd4s PP, the energy "levels", not bands, of Ti 3s and 3p states, are located at -2.0 Hr and -1.2 Hr, respectively. This result suggests that the Ti 3s and 3p orbitals do not make any hybridization but only give Coulomb repulsions with the O orbitals as well as the Ba orbitals. In the DOS with the Ti3d4s PP, on the other hand, the energy levels of Ti 3s and 3p states are not shown because Ti 3s and 3p states were treated as the core charges. This result means that the Ti 3s and 3p orbitals cannot even give Coulomb repulsions with the O orbitals as well as the Ba orbitals.

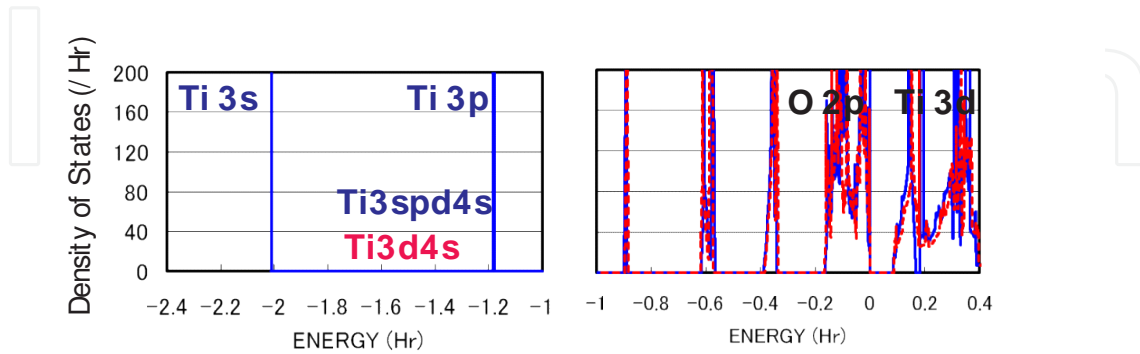


Figure 3. Total density of states (DOS) of fully optimized tetragonal BaTiO_3 with the Ti3spd4s PP (solid line) and cubic BaTiO_3 with the Ti3d4s PP (red dashed line) [11].

Another viewpoint is about the Coulomb repulsions between Ti 3s and $3p_{x(y)}$ states and $\text{O}_{x(y)}$ 2s and $2p_{x(y)}$ states in tetragonal BaTiO_3 . Figure 4(a) and 4(b) show two-dimensional electron-density contour map on the xz -plane. These are the optimized calculated results with a fixed to be 3.8 Å, and the electron density in Fig. 4(a) is quantitatively in good agreement with the experimental result [22]. The electron density between Ti and O_x ions in Fig. 3(a) is larger than that in Fig. 4(b), which suggests that Ti ion displacement is closely related to the Coulomb repulsions between Ti 3s and $3p_{x(y)}$ states and $\text{O}_{x(y)}$ 2s and $2p_{x(y)}$ states; the Ti-O Coulomb repulsion is an important role in the appearance of the ferroelectric state in BaTiO_3 .

The present discussion of the Coulomb repulsions is consistent with the previous reports. A recent soft mode investigation [8] of BaTiO_3 shows that Ba ions contribute little to the appearance of Ti ion displacement along the [001] axis. This result suggests that Ti ion displacement is closely related to the structural distortion of TiO_6 octahedra. In the present calculations, on the other hand, the only difference between BaTiO_3 with the Ti3spd4s PP and with the Ti3d4s PP is the difference in the expression for the Ti 3s and 3p states, *i.e.*, the explicit treatment and including core charges. However, our previous calculation [20] shows that the strong Coulomb repulsions between Ti 3s and $3p_z$ states and O_z 2s and $2p_z$ states do not favor Ti ion displacement along the [001] axis. This result suggests that the Coulomb repulsions between Ti 3s and $3p_{x(y)}$ states and $\text{O}_{x(y)}$ 2s and $2p_{x(y)}$ states would contribute to Ti ion displacement along the [001] axis, and the suggestion is consistent with a recent calculation [9] for PbTiO_3 indicating that the tetragonal and ferroelectric structure appears more favorable as the a lattice constant decreases.

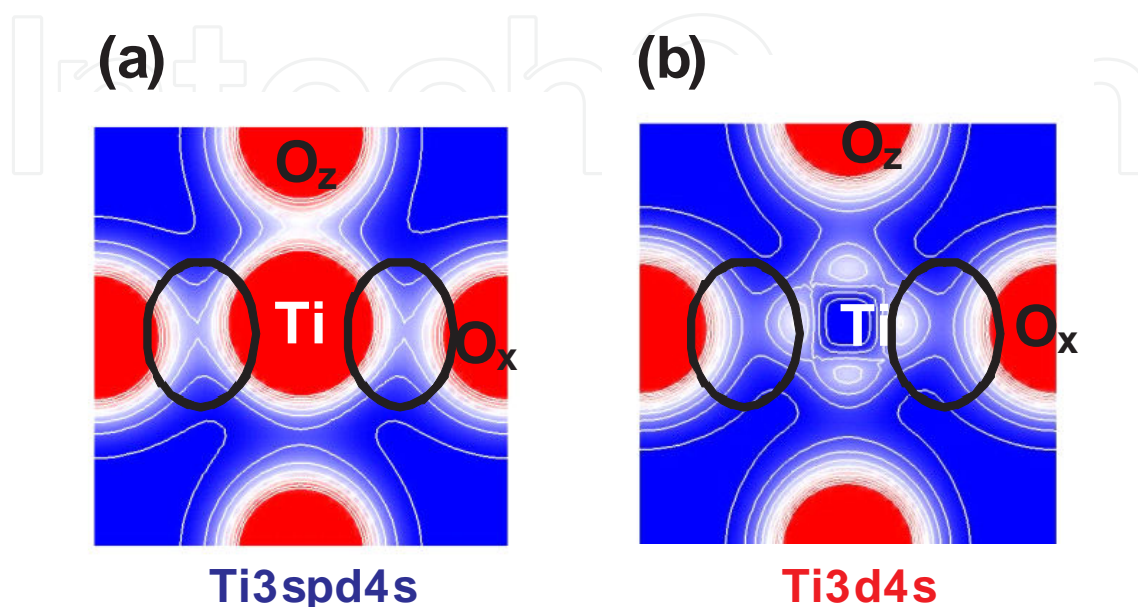


Figure 4. Two-dimensional electron-density contour map on the xz -plane for tetragonal BaTiO_3 : (a) with the Ti3spd4s PP, and (b) with the Ti3d4s PP. The optimized calculated results with a fixed to be 3.8 \AA are shown in both figures. The electron density increases as color changes from blue to red via white. Contour curves are drawn from 0.4 to 2.0 e/\AA^3 with increments of 0.2 e/\AA^3 [11].

Considering the above investigations, we propose the mechanism of Ti ion displacement as follows: Ti ion displacement along the z -axis appears when the Coulomb repulsions between Ti $3s$ and $3 p_{x(y)}$ states and $\text{O}_{x(y)}$ $2s$ and $2 p_{x(y)}$ states, in addition to the dipole-dipole interaction, overcome the Coulomb repulsions between Ti $3s$ and $3p_z$ states and O_z $2s$ and $2p_z$ states. An illustration of the Coulomb repulsions is shown in Fig. 5(a). In fully optimized BaTiO_3 with the Ti3spd4s PP, the Ti ion can be displaced due to the above mechanism. In fully optimized BaTiO_3 with the Ti3d4s PP, on the other hand, the Ti ion cannot be displaced due to the weaker Coulomb repulsions between Ti and $\text{O}_{x(y)}$ ions. However, since the Coulomb repulsion between Ti and O_z ions in BaTiO_3 with the Ti3d4s PP is also weaker than that in BaTiO_3 with the Ti3spd4s PP, the Coulomb repulsions between Ti and $\text{O}_{x(y)}$ ions in addition to the log-range force become comparable to the Coulomb repulsions between Ti and O_z ions both in Ti PPs, as the a lattice parameter becomes smaller. The above discussion suggests that the hybridization between Ti $3d$ and O_z $2s$ and $2p_z$ stabilizes Ti ion displacement, but contribute little to a driving force for the appearance of Ti ion displacement.

It seems that the above proposed mechanism for tetragonal BaTiO₃ can be applied to the mechanism of Ti ion displacement in rhombohedral BaTiO₃, as illustrated in Fig. 5(b). The strong isotropic Coulomb repulsions between Ti 3s and 3p_x (y, z) states and O_x (y, z) 2s and 2p_x (y, z) states yield Ti ion displacement along the [111] axis. On the other hand, when the isotropic Coulomb repulsions are weaker or stronger, the Ti ion cannot be displaced and therefore it is favoured for the crystal structure to be cubic.

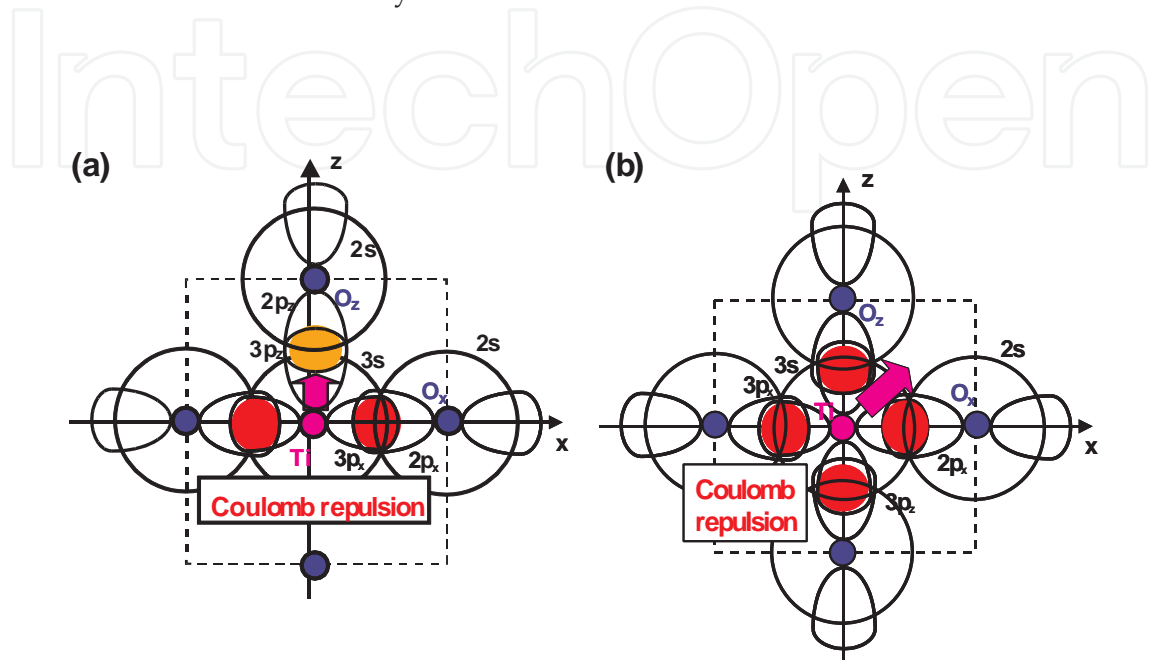


Figure 5. Illustrations of the proposed mechanisms for the Coulomb repulsions between Ti 3s and 3p states and O 2s and 2p states in BaTiO₃: (a) anisotropic Coulomb repulsions between Ti 3s and 3p_x (y) states and O_x (y) 2s and 2p_x (y) states, and between Ti 3s and 3p_z states and O_z 2s and 2p_z states, in the tetragonal structure. (b) isotropic Coulomb repulsions between Ti 3s and 3p_x (y, z) states and O_x (y, z) 2s and 2p_x (y, z) states, in the rhombohedral structure [11].

Let us investigate the structural properties of rhombohedral BaTiO₃. Figures 6(a) and 6(b) show the optimized results of the $90-\alpha$ degree and δ_{Ti} as a function of V of fixed volumes of the unit cells in rhombohedral BaTiO₃, respectively, where α denotes the angle between two lattice vectors. In these figures, α denotes the angle between two crystal axes of rhombohedral BaTiO₃, and δ_{Ti} denotes the value of the Ti ion displacement along the [111] axis. Results with arrows are the fully optimized results; V_{opt} denote the volume of the fully optimized unit cell with the Ti3spd4s PP. The other results are those with all the inner coordination optimized with fixed volumes of the unit cells. The proposal mechanisms about the Coulomb repulsions seem to be consistent with the calculated results shown in Fig.6: For $V/V_{\text{opt}} \lesssim 0.9$ or $\gtrsim 1.3$, the isotropic Coulomb repulsions are weaker or stronger, and the Ti ion cannot be displaced along the [111] axis and therefore the crystal structure is cubic for both Ti PPs. For $0.9 \lesssim V/V_{\text{opt}} \lesssim 1.3$, on the other hand, the isotropic Coulomb repulsions are strong enough to yield Ti ion displacement for both Ti PPs. However, since the magnitude of the isotropic Coulomb repulsion is different in the two Ti PPs, the properties of the $90-\alpha$ degree and δ_{Ti} are different quantitatively.

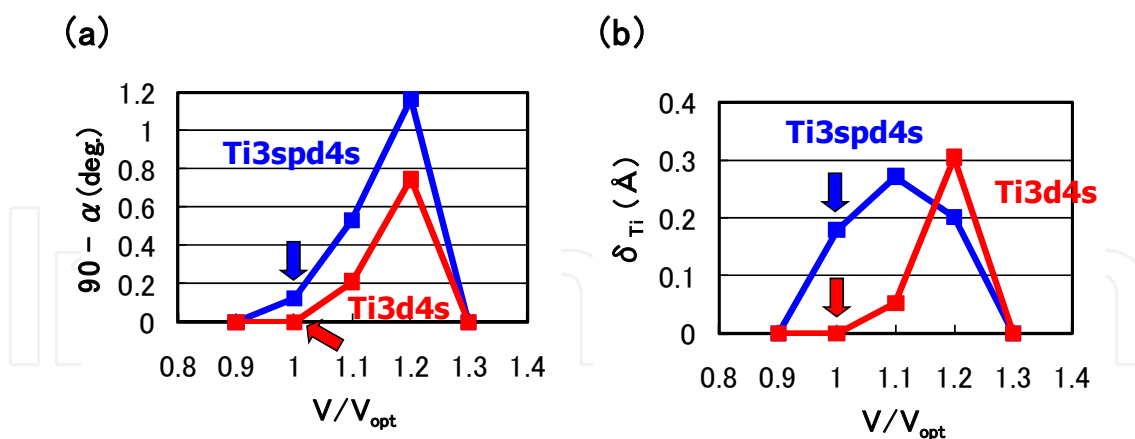


Figure 6. Optimized calculated results as a function of the fixed volumes of the unit cells in rhombohedral BaTiO₃: (a) $90 - \alpha$ degree and (b) δ_{Ti} to the [111] axis. Blue lines correspond to the results with the Ti3spd4s PP, and red lines correspond to those with the Ti3d4s PP. V_{opt} denote the volume of the fully optimized unit cell with the Ti3spd4s PP. Results with arrows are the fully optimized results, and the other results are those with all the inner coordination optimized for fixed volumes of the unit cells [11].

3.1.2. Role of Zn 3s, 3p and 3d states in ferroelectric $BiZn_{0.5}Ti_{0.5}O_3$

As discussed in Sec. 3.1.1, the Coulomb repulsions between Ti 3s and $3p_{x(y)}$ states and $O_{x(y)}$ 2s and $2p_{x(y)}$ states have an important role in the appearance of the ferroelectric state in tetragonal BaTiO₃. In this subsection, we discuss the role of Zn 3d (d^{10}) states in addition to 3s and 3p states for ferroelectricity in tetragonal BZT.

Table 1 shows a summary of the optimized results of BZT in Cases I and II. ΔE_{total} denotes the difference in total energy per f.u. between the rhombohedral and other structures. Although the lattice constant in each structure except the rhombohedral one seems to be quantitatively similar in both cases, properties of ΔE_{total} are different. In Case I, the rhombohedral structure is the most stable, which is in disagreement with the experimental result [24]. In Case II, on the other hand, the monoclinic structure, which is the "pseudo-C-type-tetragonal" structure, is the most stable. Unfortunately, this result seems to be in disagreement with the experimental result [24], but is in good agreement with the recent calculated result [6]. Note that the magnitude of ΔE_{total} in Case II is markedly smaller than that in Case I. In contrast to BZT, the rhombohedral structure is the most stable structure in both cases in BMT, which is consistent with the experimental result [26].

Figures 7(a) and 7(b) show two-dimensional electron density contour maps of the C-type tetragonal BZT in Cases I and II, respectively. The Coulomb repulsion of Zn-O_x in Case II is larger than that in Case I, and the Coulomb repulsion favorably causes Zn ion displacement to O_z in Case II. This result is consistent with Sec. 3.1.1. In contrast to the properties of Zn-O bonding, the inner coordination of the Ti ion is similar in both cases, although the electron densities are markedly different. This result suggests that the Coulomb repulsion magnitude of Ti-O_z is the same as that of Ti-O_x in small Ti-O bonding (≈ 1.8 Å), in both Cases I and II. Figures 7(c) and 7(d) show two-dimensional electron density contour maps of the C-type tet-

agonal BMT in Cases I and II, respectively. Although the electron densities in both cases are markedly different, the inner coordination of the Mg ion are similar. This result suggests that the Coulomb repulsion between Mg and O is not strong sufficiently for inducing Mg ion displacement even in Case II.

Structure	a (Å)	c (Å)	c/a	α (deg.)	ΔE_{total} (eV/f.u.)
A-type Tetra.	3.748	4.579	1.222	90	0.316
C-type Tetra.	3.681	4.784	1.299	90	0.240
G-type Tetra.	3.725	4.574	1.228	90	0.158
Monoclinic	3.735	4.741	1.269	$\beta = 91.5$	0.193
Rhombohedral	5.560		1	59.93	0
Experiment [24]	3.822	4.628	1.211	90	---

(a)

Structure	a (Å)	c (Å)	c/a	α (deg.)	ΔE_{total} (eV/f.u.)
A-type Tetra.	3.711	4.662	1.256	90	0.135
C-type Tetra.	3.670	4.789	1.305	90	0.091
G-type Tetra.	3.684	4.698	1.275	90	0.047
Monoclinic	3.726	4.740	1.272	$\beta = 91.1$	-0.021
Rhombohedral	5.590		1	59.90	0
Experiment [24]	3.822	4.628	1.211	90	---

(b)

Table 1. Summary of the optimized results of BZT in (a) Case I and (b) Case II. a and c denote the lattice parameters, and α and β denote angles between two lattice axes. ΔE_{total} denotes the difference in total energy per f.u. between the rhombohedral and other structures [10].

Finally in this subsection, we discuss the difference in the electronic structures between the C-type tetragonal and the monoclinic BZT. Figures 8(a) and 8(b) show the electron density contour maps of the C-type tetragonal BZT and that of the monoclinic BZT in Case II, respectively. This result suggests that the strong Coulomb repulsion between Zn and O_z causes the small Zn ion displacement in the [110] direction in the monoclinic BZT, which makes the Coulomb repulsion of Zn- O_z weaker than that in the C-type tetragonal BZT. As a result, this small Zn ion displacement makes the monoclinic BZT more stable than the C-type tetragonal structure.

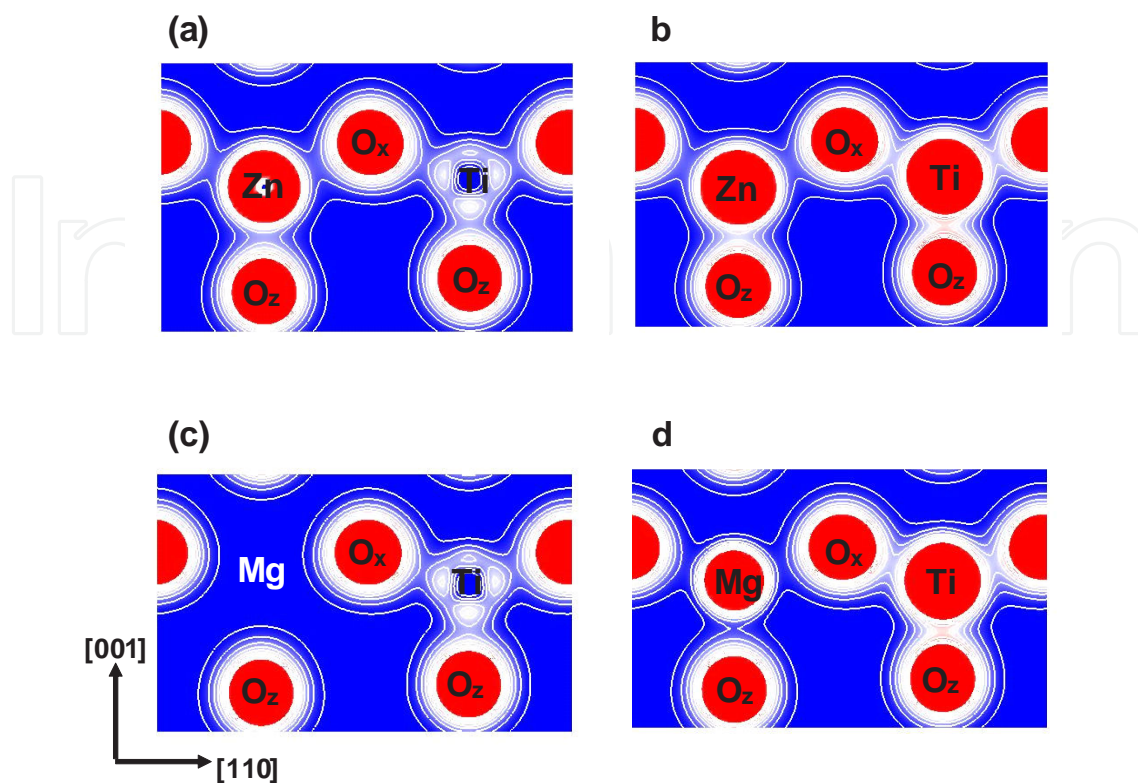


Figure 7. Two-dimensional electron density contour maps of monoclinic (a) BZT in Case I, (b) BZT in Case II, (c) BMT in Case I, and (d) BMT in Case II. The electron density increases as color changes from blue to red via white. Contour curves are drawn from 0.2 to 2.0 $e/\text{\AA}^3$ with increments of 0.2 $e/\text{\AA}^3$ [10].

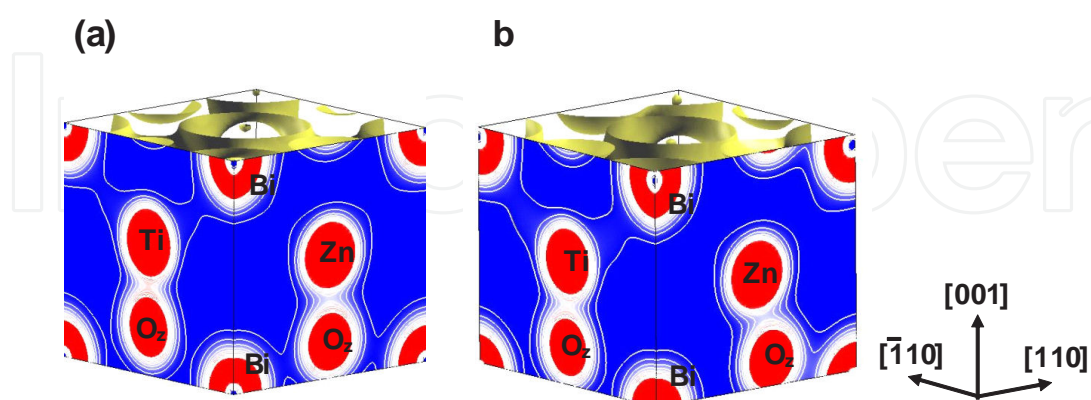


Figure 8. Two-dimensional electron density contour maps of BZT in Case II (a) C-type tetragonal and (b) monoclinic. The electron density increases as color changes from blue to red via white. Contour curves are drawn from 0.2 to 2.0 $e/\text{\AA}^3$ with increments of 0.2 $e/\text{\AA}^3$ [10].

3.2. Piezoelectricity

3.2.1. Role of the Ti-O Coulomb repulsions in tetragonal piezoelectric SrTiO_3 and BaTiO_3

As discussed in Sec. 3.1, the Coulomb repulsions between Ti 3s and $3p_{x(y)}$ states and $O_{x(y)}$ 2s and $2p_{x(y)}$ states have an important role in the appearance of the ferroelectric state in tetragonal BaTiO_3 . In this subsection, we discuss the role of the Ti-O Coulomb repulsions for piezoelectric SrTiO_3 and BaTiO_3 .

Figure 9(a) shows the optimized results for $c - c_{\text{cub}}$ as a function of the a lattice parameters in tetragonal SrTiO_3 and BaTiO_3 , where c_{cub} denotes the c lattice parameter in cubic SrTiO_3 and BaTiO_3 , respectively. These results are the fully optimized results and the results with the c lattice parameters and all the inner coordination optimized for fixed a . The fully optimized parameters of SrTiO_3 ($a = 3.84 \text{ \AA}$: cubic) and BaTiO_3 ($a = 3.91 \text{ \AA}$ and $c = 4.00 \text{ \AA}$: tetragonal) are within 2.0 % in agreement with the experimental results in room temperature. Figure 9(b) shows the evaluated results for P_3 as a function of the a lattice parameters in tetragonal SrTiO_3 and BaTiO_3 , where P_3 , which is evaluated by Eq. (2), denotes the spontaneous polarization along the [001] axis. Note that the tetragonal and ferroelectric structures appear even in SrTiO_3 when the fixed a lattice parameter is compressed to be smaller than the fully-optimized a lattice parameter. As shown in Figs. 9(a) and 9(b), the tetragonal and ferroelectric structure appears more favorable as the fixed a lattice parameter decreases, which is consistent with previous calculated results [9, 11]. The results would be due to the suggestion discussed in the previous section that the large Coulomb repulsion of Ti-O bonding along the [100] axis (and the [010] axis) is a driving force of the displacement of Ti ions along the [001] axis, *i.e.*, the large Coulomb repulsion along the [100] axis (and the [010] axis) is essential for the appearance of the tetragonal structure.

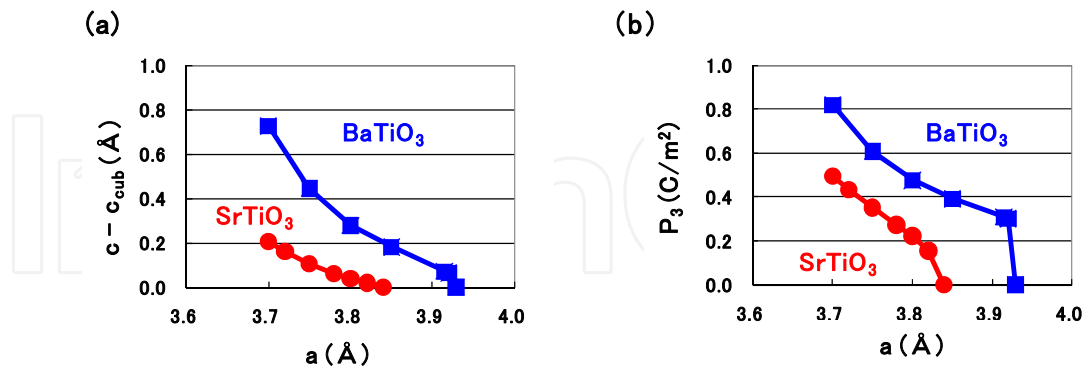


Figure 9. Optimized calculated results as a function of a lattice parameters in compressive tetragonal SrTiO_3 and BaTiO_3 : (a) $c - c_{\text{cub}}$ and (b) P_3 , *i.e.*, spontaneous polarization along the [001] axis [12].

In the following, we use $c - c_{\text{cub}}$ as a functional parameter, because $c - c_{\text{cub}}$ is closely related to η_3 . Figures 10(a) and 10(b) shows the piezoelectric properties of e_{33} and e_{31} as a function of $c - c_{\text{cub}}$ in tetragonal SrTiO_3 and BaTiO_3 . The value $c - c_{\text{cub}}$ is optimized value as shown in Fig. 9(a) and e_{33} and e_{31} are evaluated values in their optimized structures. Note that e_{33} become

larger at $c - c_{\text{cub}} \approx 0$, especially in SrTiO₃. These properties seem to be similar to the properties around the Curie temperatures in piezoelectric ABO₃; Damjanovic emphasized the importance of the polarization extension as a mechanism of larger piezoelectric constants in a recent paper [28]. Contrary to e_{33} , on the other hand, the changes in e_{31} are much smaller than the changes in e_{33} , but note that e_{31} shows negative in SrTiO₃ while positive in BaTiO₃.

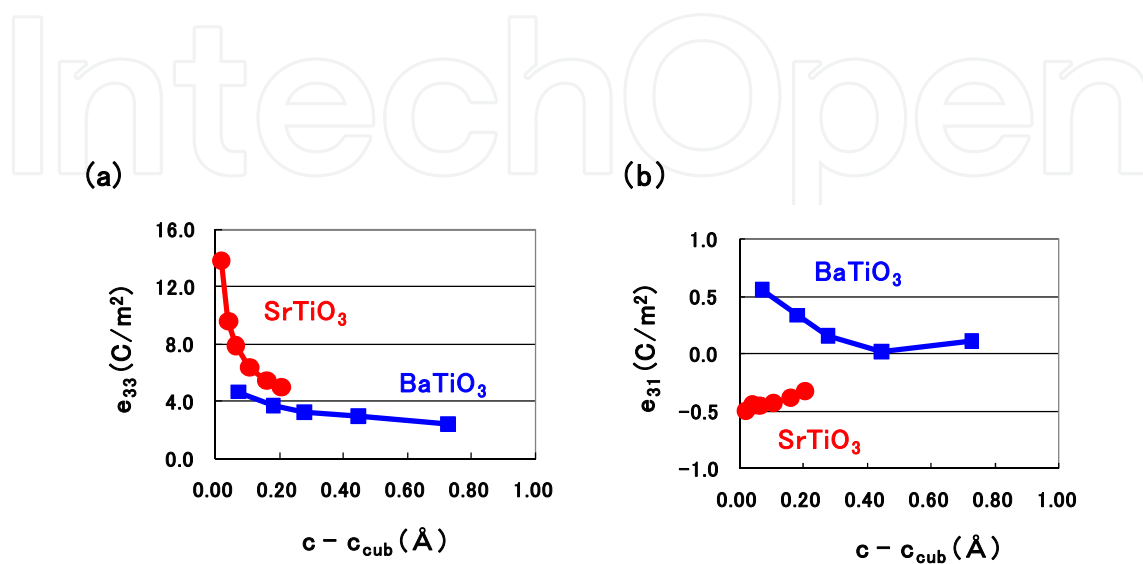


Figure 10. Evaluated piezoelectric constants as a function of $c - c_{\text{cub}}$ in optimized tetragonal SrTiO₃ and BaTiO₃: (a) e_{33} and (b) e_{31} [12].

As expressed in Eq. (3), e_{3j} is the sum of the contributions from the clamped term and the relaxed term. However, it has been generally known that the contribution to e_{3j} from the clamped term is much smaller than that from the relaxed term; in fact, the absolute values of the e_{33} clamped terms are less than 1 C/m² in both SrTiO₃ and BaTiO₃. We therefore investigate the contributions to the relaxed term of e_{33} and e_{31} in detail. As expressed in Eq. (3), the relaxed terms of e_{3j} are proportional to the sum of the products between the $Z_{33}^*(k)$ and $\partial u_3(k)/\partial \eta_j$ ($j = 3$ or 1) values. Let us show the evaluated results of $Z_{33}^*(k)$, $\partial u_3(k)/\partial \eta_3$, and $\partial u_3(k)/\partial \eta_1$ in the following. Figures 11(a) and 11(b) show the $Z_{33}^*(k)$ values in SrTiO₃ and BaTiO₃, respectively. Properties of the $Z_{33}^*(k)$ values are quantitatively similar in both SrTiO₃ and BaTiO₃. Therefore, the difference in the properties of e_{33} and e_{31} between SrTiO₃ and BaTiO₃ must be due to the difference in the properties of $\partial u_3(k)/\partial \eta_j$. Figures 12(a) and 12(b) show the $\partial u_3(k)/\partial \eta_3$ values in SrTiO₃ and BaTiO₃, respectively. In these figures, O_x and O_z denote oxygen atoms along the [100] and [001] axes, respectively. Clearly, the absolute values of $\partial u_3(k)/\partial \eta_3$ are different in between SrTiO₃ and BaTiO₃. On the other hand, Figs. 13(a) and 13(b) show the $\partial u_3(k)/\partial \eta_1$ values in SrTiO₃ and BaTiO₃, respectively. The absolute values of $\partial u_3(k)/\partial \eta_1$, especially for Ti, O_x, and O_z are different in between SrTiO₃ and BaTiO₃. As a result, the quantitative differences in e_{33} and e_{31} between SrTiO₃ and BaTiO₃ are due to the differences in the contribution of the $\partial u_3(k)/\partial \eta_3$ and $\partial u_3(k)/\partial \eta_1$ values, respectively.

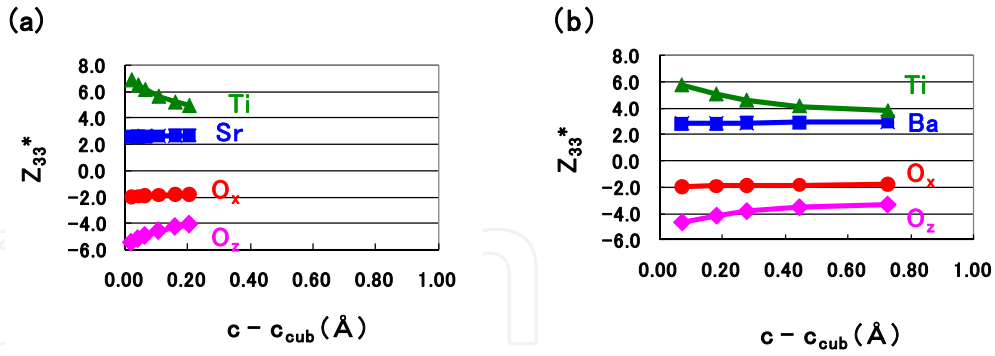


Figure 11. Evaluated Born effective charges $Z_{33}^*(k)$ as a function of $c - c_{\text{cub}}$: (a) SrTiO_3 and (b) BaTiO_3 . O_x and O_z denote oxygen atoms along the $[100]$ axis and the $[001]$ axis, respectively [12].

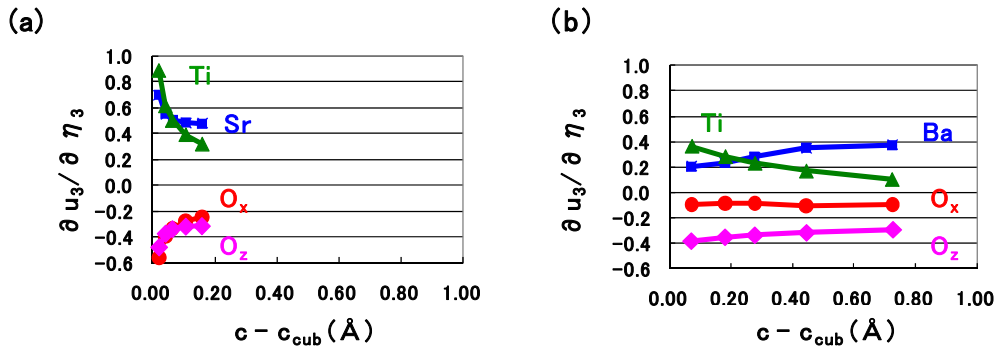


Figure 12. Evaluated values of $\partial u_3(k)/\partial \eta_3$ as a function of $c - c_{\text{cub}}$: (a) SrTiO_3 and (b) BaTiO_3 [12].

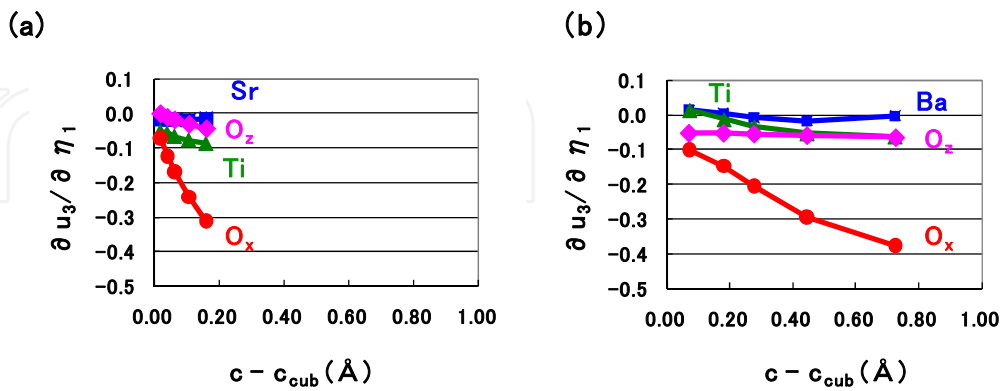


Figure 13. Evaluated values of $\partial u_3(k)/\partial \eta_1$ as a function of $c - c_{\text{cub}}$: (a) SrTiO_3 and (b) BaTiO_3 [12].

Let us discuss the reasons of the quantitative differences in e_{33} between SrTiO_3 and BaTiO_3 . Figure 14(a) shows the difference between the Ti- O_z distance ($R_{\text{Ti-O}_z}$) and the sum of the r_{Ti}

and r_{O_z} ($r_{Ti} + r_{O_z}$) along the [001] axis as a function of $c - c_{cub}$. Note that R_{Ti-O_z} is smaller than $r_{Ti} + r_{O_z}$ in both SrTiO₃ and BaTiO₃. However, the difference in absolute value between R_{Ti-O_z} and $r_{Ti} + r_{O_z}$ in SrTiO₃ is smaller than the difference in BaTiO₃ for $0 \lesssim c - c_{cub} \lesssim 0.20$. This result suggests that the Ti-O_z Coulomb repulsion along the [001] axis in SrTiO₃ is smaller than that in BaTiO₃ and that therefore the Ti ion of SrTiO₃ can be displaced more easily along the [001] axis than that of BaTiO₃. This would be a reason why the absolute values of $\partial u_3(k)/\partial \eta_3$ of Ti and O_z ions in SrTiO₃ are larger than that in BaTiO₃. Figure 14(b) shows the difference between the A-O_x distance (R_{A-O_x}) and the sum of r_A and r_{O_x} ($r_A + r_{O_x}$) on the (100) plane as a function of $c - c_{cub}$, where the values of the ionic radii are defined as Shannon's ones [23]. Note that R_{A-O_x} is smaller than $r_A + r_{O_x}$ in both SrTiO₃ and BaTiO₃. However, the difference in absolute value between R_{A-O_x} and $r_A + r_{O_x}$ in SrTiO₃ is much smaller than the difference in BaTiO₃ for $0 \lesssim c - c_{cub} \lesssim 0.20$. This result suggests that the Sr-O_x Coulomb repulsion on the (100) plane in SrTiO₃ is much smaller than the Ba-O_x Coulomb repulsion in BaTiO₃ and that therefore Sr and O_x ions of SrTiO₃ can be displaced more easily along the [001] axis than Ba and O_x ions of BaTiO₃. This would be a reason why the absolute values of $\partial u_3(k)/\partial \eta_3$ of Sr and O_x ions in SrTiO₃ are larger than those of Ba and O_x ions in BaTiO₃.

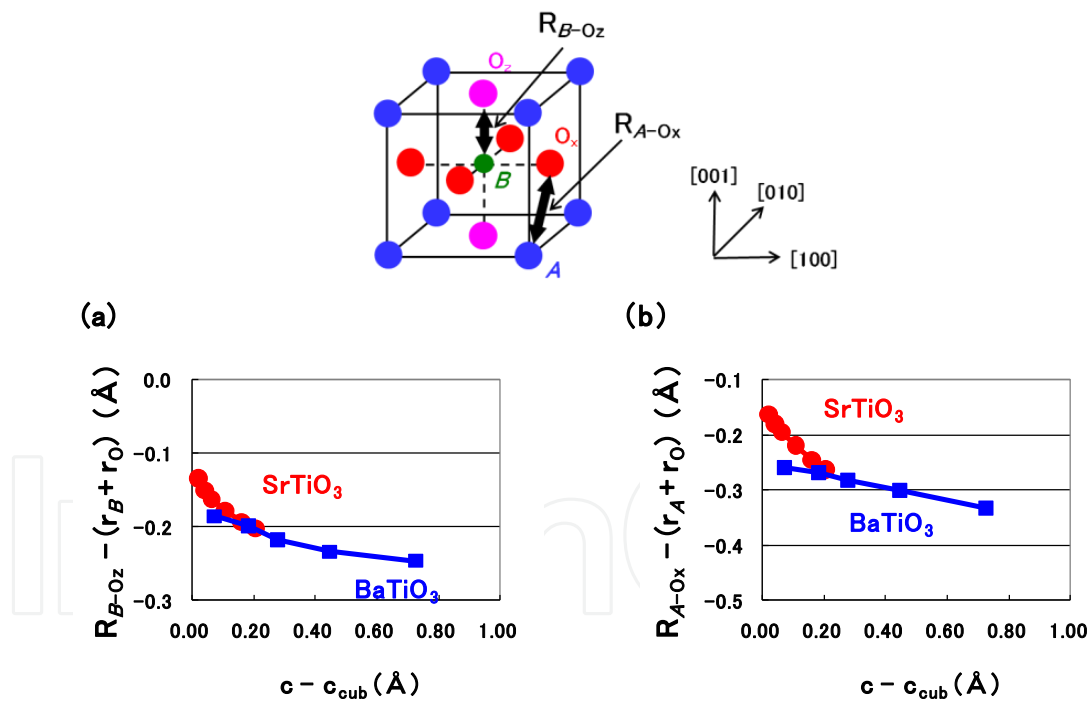


Figure 14. Evaluated values as a function of $c - c_{cub}$ in optimized tetragonal SrTiO₃ and BaTiO₃: (a) difference between the Ti-O_z distance (R_{Ti-O_z}) and $r_{Ti} + r_{O_z}$. (b) difference between the A-O_x distance (R_{A-O_x}) and $r_A + r_{O_x}$. R_{A-O_x} and R_{Ti-O_z} in ATiO₃ are also illustrated. Note that all the ionic radii are much larger and that A and Ti ions are displaced along the [001] axis in actual ATiO₃ [12].

Finally, in this subsection, we discuss the relationship between $\partial u_3(k)/\partial \eta_3$ and $c - c_{cub}$ in detail. Figure 15(a) shows the differences in the total energy (ΔE_{total}) as a function of $u_3(Ti)$. In

this figure, the properties of SrTiO₃ with $\eta_3 = 0.011$, SrTiO₃ with $\eta_3 = 0.053$ and fully optimized BaTiO₃ as a reference, are shown. Calculations of E_{total} were performed with the fixed crystal structures of previously optimized structures except Ti ions. Clearly, the magnitude of $u_3(\text{Ti})$ at the minimum points of the ΔE_{total} and the depth of the potential are closely related to the spontaneous polarization P_3 and the Curie temperature (T_C), respectively. On the other hand, e_{33} seems to be closely related to the deviation at the minimum points of the ΔE_{total} . Figure 15(b) shows illustrations of ΔE_{total} curves with deviations at the minimum points of the ΔE_{total} values, corresponding to the ΔE_{total} curves of SrTiO₃ in Fig. 15(a). Clearly, as η_3 becomes smaller, the deviated value at the minimum point of the ΔE_{total} values becomes smaller, *i.e.*, the Ti ion can be displaced more favourably. On the other hand, as shown in Fig. 12(a), the absolute value of $\partial u_3(\text{Ti})/\partial \eta_3$ becomes larger as η_3 becomes smaller.

Therefore, the Ti ion can be displaced more favourably as the deviated value at the minimum point of the ΔE_{total} values becomes smaller. The relationship between e_{33} and $\partial u_3(\text{Ti})/\partial \eta_3$ is discussed in Sec. 3.2.3.

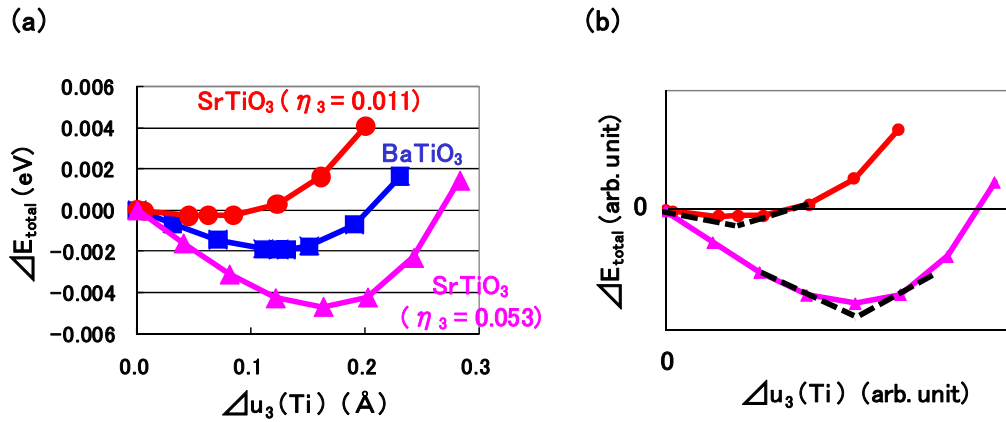


Figure 15. a) ΔE_{total} as a function of $u_3(\text{Ti})$ in tetragonal SrTiO₃ and BaTiO₃. (b) Illustration of the ΔE_{total} curves in tetragonal SrTiO₃ with $\eta_3 = 0.011$ and SrTiO₃ with $\eta_3 = 0.053$ with deviations at the minimum point of ΔE_{total} [14].

3.2.2. Proposal of new piezoelectric materials

The previous discussion in Sec. 3.2.1 suggests that the piezoelectric properties of e_{33} are closely related to the B - X Coulomb repulsions in tetragonal ABX_3 . In the viewpoint of the change of the B - X Coulomb repulsions, we recently proposed new piezoelectric materials [16, 17], *i.e.*, BaTi_{1-x}Ni_xO₃ and Ba(Ti_{1-3z}Nb_{3z})(O_{1-z}N_z)₃.

It has been known that BaNiO₃ shows the 2H hexagonal structure as the most stable structure in room temperature. Moreover, the ionic radius of Ni⁴⁺ (d^6) with the low-spin state in 2H BaNiO₃ is 0.48 Å, which is much smaller than that of Ti⁴⁺ (d^0), 0.605 Å, in BaTiO₃. Therefore, due to the drastic change in the (Ti_{1-x}Ni_x)-O Coulomb repulsions in tetragonal BaTi_{1-x}Ni_xO₃, the e_{33} piezoelectric values are expected to be larger than that in tetragonal BaTiO₃, especially around the morphotropic phase boundary (MPB). Figure 16(a) shows the total-en-

ergy difference ΔE_{total} between 2H and tetragonal structures of BaTi_{1-x}Ni_xO₃ as a function of x . The most stable structure changes at $x \approx 0.26$. Figure 16(b) shows $c - c_{\text{cub}}$ as a function of x . The $c - c_{\text{cub}}$ value shows 0 around $x = 0.26$, which suggests the appearance of the MPB, *i.e.*, the e_{33} piezoelectric value shows a maximum at $x \approx 0.26$.

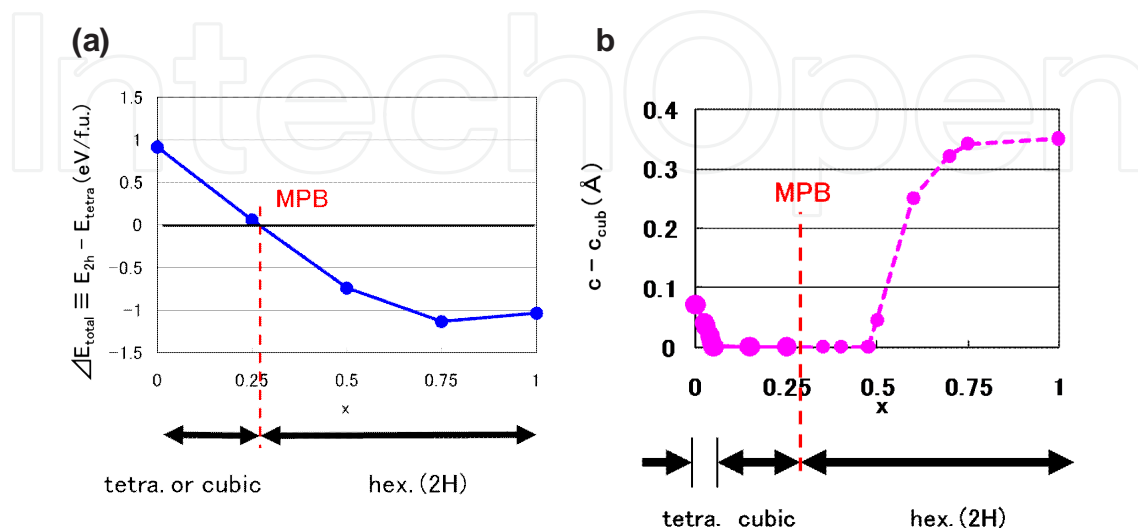


Figure 16. a) ΔE_{total} (total-energy difference between 2H and tetragonal structures), and (b) $c - c_{\text{cub}}$ of the tetragonal structure, as a function of x in BaTi_{1-x}Ni_xO₃ [16]. For $0.26 \leq x \leq 1$, the tetragonal structure is not the most stable one.

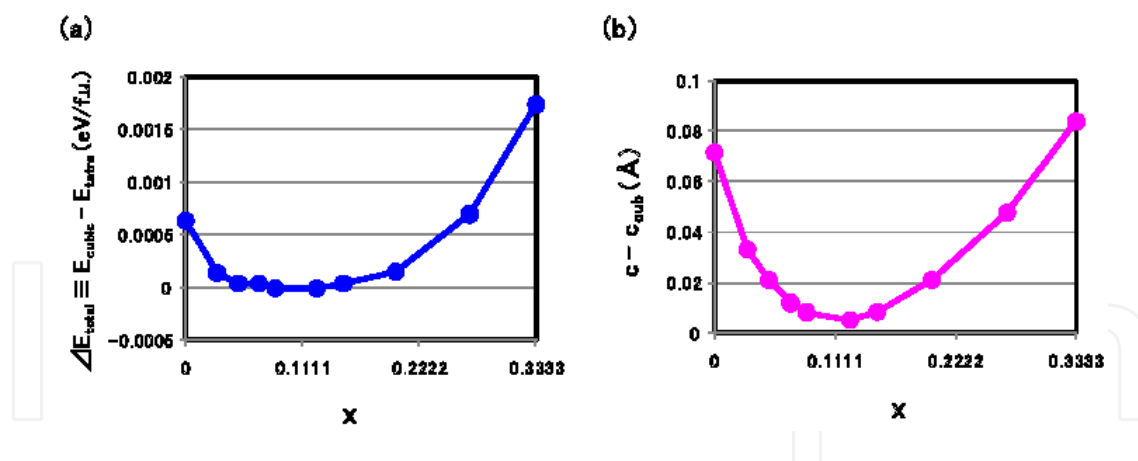


Figure 17. (a) ΔE_{total} (total-energy difference between cubic and tetragonal structures), and (b) $c - c_{\text{cub}}$, as a function of x in Ba(Ti_{1-3z}Nb_{3z})(O_{1-z}N_z)₃ [17].

Another proposal is tetragonal Ba(Ti_{1-3z}Nb_{3z})(O_{1-z}N_z)₃, which consists of BaTiO₃ and BaNbO₂N [17]. Due to the change of (Ti_{1-3z}Nb_{3z})-(O_{1-z}N_z) Coulomb repulsions, the e_{33} piezoelectric values are expected to be larger than that in tetragonal BaTiO₃. Recent experimental paper reported that the most stable structure of BaNbO₂N is cubic in room temperature [34]. Contrary to the experimental result, however, our calculations suggest that the tetragonal structure will be more stable than the cubic one, as shown in Fig. 17(a). Figure 17(b) shows $c - c_{\text{cub}}$

as a function of x . The $c - c_{\text{cub}}$ value shows almost 0 at $x \approx 0.12$. Although the MPB does not appear in tetragonal $\text{Ba}(\text{Ti}_{1-3z}\text{Nb}_{3z})(\text{O}_{1-z}\text{N}_z)_3$, the e_{33} piezoelectric values are expected to show a maximum at $x \approx 0.12$.

3.2.3. Piezoelectric properties of in tetragonal ABX_3

In the following, we discuss the role of the B - X Coulomb repulsions in piezoelectric ABX_3 .

Figures 18(a) and 18(b) show the piezoelectric properties of e_{33} as a function of the value $c - c_{\text{cub}}$ in tetragonal ABX_3 , where c_{cub} denotes the c lattice parameter in cubic ABX_3 ; $c - c_{\text{cub}}$ is a closely related parameter to η_3 . For ABX_3 , SrTiO_3 , BaTiO_3 and PbTiO_3 with the c lattice parameter and all the inner coordination optimized for fixed a , and $\text{BaTi}_{1-x}\text{Ni}_x\text{O}_3$ ($0 \leq x \leq 0.05$), $\text{Ba}(\text{Ti}_{1-3z}\text{Nb}_{3z})(\text{O}_{1-z}\text{N}_z)_3$ ($0 \leq z \leq 0.125$), $\text{Ba}_{1-y}\text{Sr}_y\text{TiO}_3$ ($0 \leq y \leq 0.5$), $\text{BaTi}_{1-x}\text{Zr}_x\text{O}_3$ ($0 \leq x \leq 0.06$), and $\text{BiM}'\text{O}_3$ ($M' = \text{Al}, \text{Sc}$) with fully optimized, were prepared [15]. Note that e_{33} becomes larger as $c - c_{\text{cub}}$ becomes smaller and that the trend of e_{33} is almost independent of the kind of A ions. Moreover, note also that e_{33} of $\text{BaTi}_{1-x}\text{Ni}_x\text{O}_3$ and that of $\text{Ba}(\text{Ti}_{1-3z}\text{Nb}_{3z})(\text{O}_{1-z}\text{N}_z)_3$ show much larger values than the other ABX_3 .

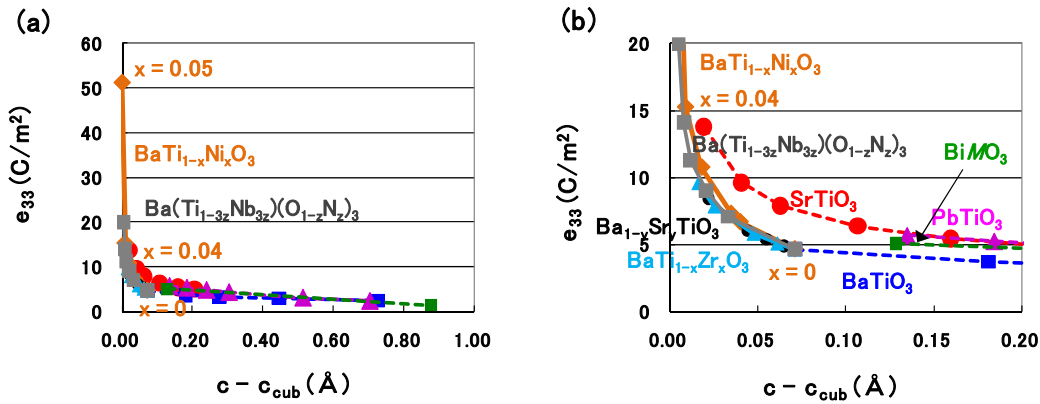


Figure 18. e_{33} as a function of $c - c_{\text{cub}}$ for different scales [15].

Let us discuss the relationship between $\partial u_3(k)/\partial \eta_3$ and $c - c_{\text{cub}}$ in $\text{BaTi}_{1-x}\text{Ni}_x\text{O}_3$ and BaTiO_3 in the following. Figures 19(a) and 19(b) show the $\partial u_3(k)/\partial \eta_3$ values. In these figures, O_x and O_z denote oxygen atoms along the [100] and [001] axes, respectively. Clearly, the absolute values of $\partial u_3(k)/\partial \eta_3$ in $\text{BaTi}_{1-x}\text{Ni}_x\text{O}_3$ are much larger than those in BaTiO_3 . Moreover, in comparison with Fig.18, properties of e_{33} are closely related to those of $\partial u_3(k)/\partial \eta_3$. Figure 20(a) shows the difference between $R_{B-\text{O}_z}$ and $r_B + r_{\text{O}_z}$ along the [001] axis, and Fig. 20(b) shows the difference between $R_{A-\text{O}_x}$ and $r_A + r_{\text{O}_x}$ on the (100) plane for several ABO_3 as a function of $c - c_{\text{cub}}$. Clearly, the difference between $R_{B-\text{O}_z}$ and $r_B + r_{\text{O}_z}$ is closely related to e_{33} shown in Fig. 18, rather than the difference between $R_{A-\text{O}_x}$ and $r_A + r_{\text{O}_x}$. Moreover, note that the difference in absolute value between $R_{B-\text{O}_z}$ and $r_B + r_{\text{O}_z}$ in $\text{BaTi}_{1-x}\text{Ni}_x\text{O}_3$ is much smaller than that in BaTiO_3 . This result suggests that the $(\text{Ti}_{1-x}\text{Ni}_x)\text{-O}_z$ Coulomb repulsion along the [001] axis in $\text{BaTi}_{1-x}\text{Ni}_x\text{O}_3$ is much smaller than the Ti-O_z Coulomb repulsion in BaTiO_3 and that therefore $\text{Ti}_{1-x}\text{Ni}_x$ ion of $\text{BaTi}_{1-x}\text{Ni}_x\text{O}_3$ can be displaced more easily along the [001] axis than Ti ion of

BaTiO₃. This must be a reason why the absolute value of $\partial u_3(k)/\partial \eta_3$ of Ti_{1-x}Ni_x and O_z ions in BaTi_{1-x}Ni_xO₃ is larger than those in BaTiO₃.

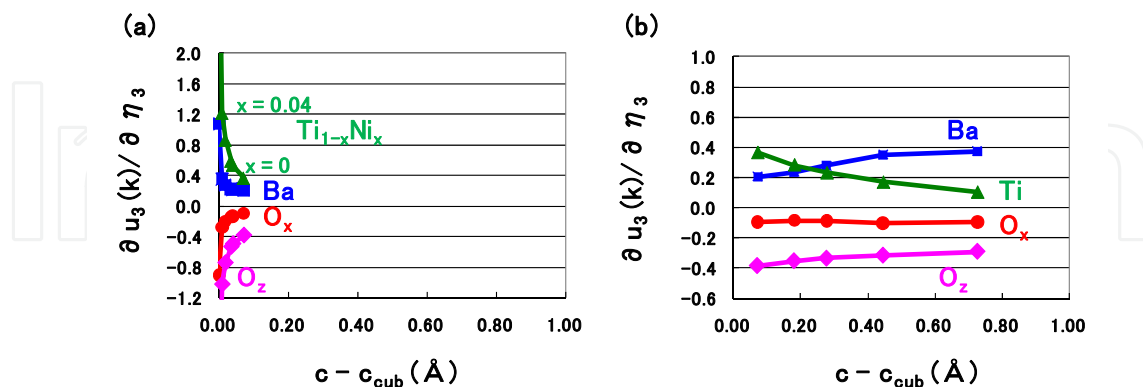


Figure 19. $\partial u_3(k)/\partial \eta_3$ as a function of $c - c_{\text{cub}}$: (a) BaTi_{1-x}Ni_xO₃ and (b) BaTiO₃ [15].

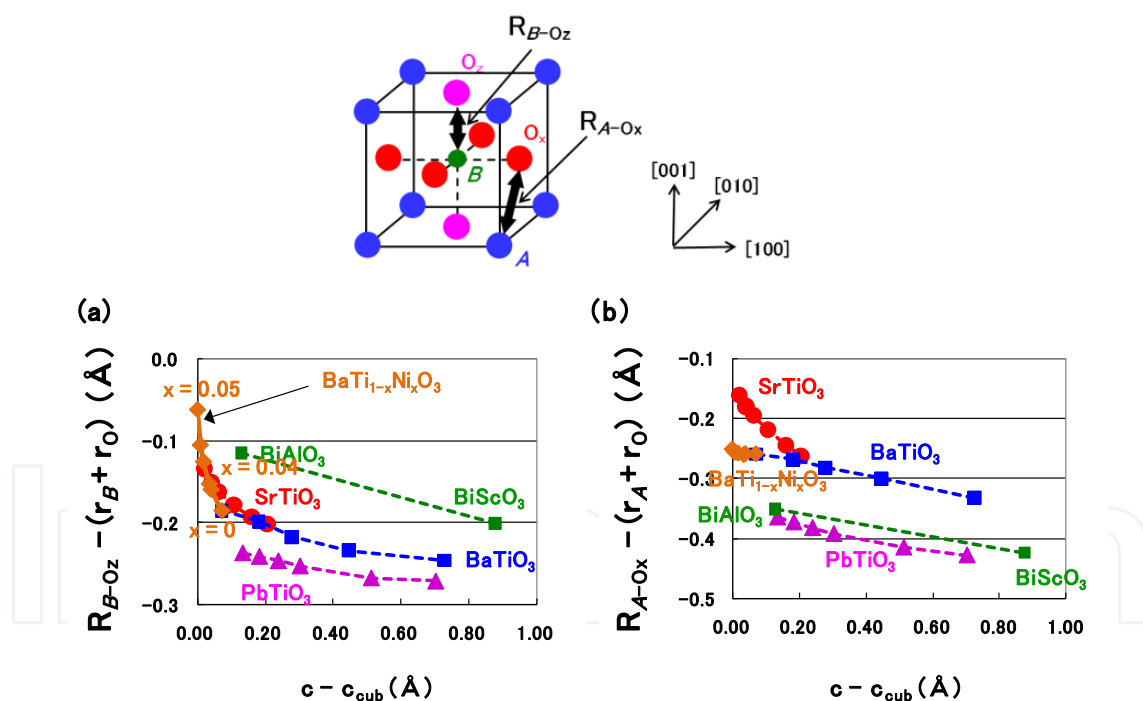


Figure 20. Evaluated values of in optimized tetragonal BaTi_{1-x}Ni_xO₃, BaTiO₃, and several ABO₃, as a function of $c - c_{\text{cub}}$: (a) $R_{B-Oz} - (r_B + r_{Oz})$, and (b) $R_{A-Ox} - (r_A + r_{Ox})$ [15].

Figure 21(a) shows ΔE_{total} as a function of the displacement of the Ti_{1-x}Ni_x ions with fixed crystal structures of fully-optimized BaTi_{1-x}Ni_xO₃. Calculations of E_{total} were performed with the fixed crystal structures of previously optimized structures except Ti_{1-x}Ni_x ions. The deviated value at the minimum point of ΔE_{total} , *i.e.*, $\partial(\Delta E_{\text{total}})/\partial u_3(\text{Ti}_{1-x}\text{Ni}_x)$, becomes

smaller as x becomes larger. Moreover, both e_{33} and $\partial u_3(\text{Ti}_{1-x}\text{Ni}_x)/\partial \eta_3$ become larger as x becomes larger, as shown in Figs. 18 and 19. This result is consistent with the result of SrTiO_3 shown in Fig. 15(a).

Let us discuss the above reasons in the following. $\partial(\Delta E_{\text{total}})/\partial u_3(\text{Ti}_{1-x}\text{Ni}_x)$ can be written as

$$\left(\frac{\partial \Delta E_{\text{total}}}{\partial u_3(\text{Ti}_{1-x}\text{Ni}_x)} \right) = \left(\frac{\partial \Delta E_{\text{total}}}{\partial \eta_3} \right) \times \left(\frac{\partial u_3(\text{Ti}_{1-x}\text{Ni}_x)}{\partial \eta_3} \right)^{-1} \quad (5)$$

As shown in Fig. 21(b), $\partial(\Delta E_{\text{total}})/\partial \eta_3$ is almost constant, and therefore, $\partial(\Delta E_{\text{total}})/\partial u_3(\text{Ti}_{1-x}\text{Ni}_x)$ is almost proportional to $(\partial u_3(\text{Ti}_{1-x}\text{Ni}_x)/\partial \eta_3)^{-1}$, i.e.,

$$\left(\frac{\partial \Delta E_{\text{total}}}{\partial u_3(\text{Ti}_{1-x}\text{Ni}_x)} \right) \propto \left(\frac{\partial u_3(\text{Ti}_{1-x}\text{Ni}_x)}{\partial \eta_3} \right)^{-1} \quad (6)$$

On the other hand, according to Eq. (3), e_{33} becomes larger as $\partial u_3(\text{Ti}_{1-x}\text{Ni}_x)/\partial \eta_3$ becomes larger. This is a reason why e_{33} becomes larger as $\partial(\Delta E_{\text{total}})/\partial u_3(\text{Ti}_{1-x}\text{Ni}_x)$ becomes smaller. This result is consistent with the result of SrTiO_3 discussed in Sec. 3.2.1.

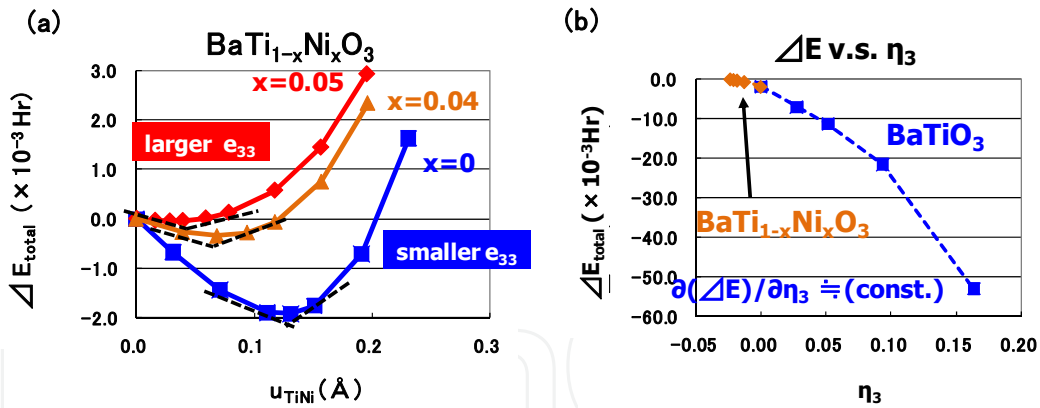


Figure 21. (a) ΔE_{total} as a function of $u_3(\text{Ti}_{1-x}\text{Ni}_x)$ in $\text{BaTi}_{1-x}\text{Ni}_x\text{O}_3$. Results with $x = 0.05, 0.04$, and 0 are shown. Dashed lines denote guidelines of $\partial(\Delta E_{\text{total}})/\partial u_3(\text{Ti}_{1-x}\text{Ni}_x)$ for each x . (b) ΔE_{total} as a function of η_3 for $\text{BaTi}_{1-x}\text{Ni}_x\text{O}_3$ and BaTiO_3 [15].

Finally, we comment on the difference in the properties between e_{33} and d_{33} in tetragonal ABX_3 . Figures 22(a) and 22(b) show the piezoelectric properties of d_{33} as a function of $c - c_{\text{cub}}$. Note that the trend of d_{33} is closely dependent on the kind of A ions. This result is in contrast with the trend of e_{33} as shown in Fig. 18. As expressed in Eq. (4), d_{33} is closely related to the elastic compliance s_{3j}^E as well as e_{3j} . In fact, the absolute value of s_{3j}^E in BiBX_3 or PbBX_3 is generally larger than that in ABX_3 with alkaline-earth A ions. This result must be due to the larger Coulomb repulsion of Bi-X or Pb-X derived from $6s$ electrons in Bi (Pb) ion.

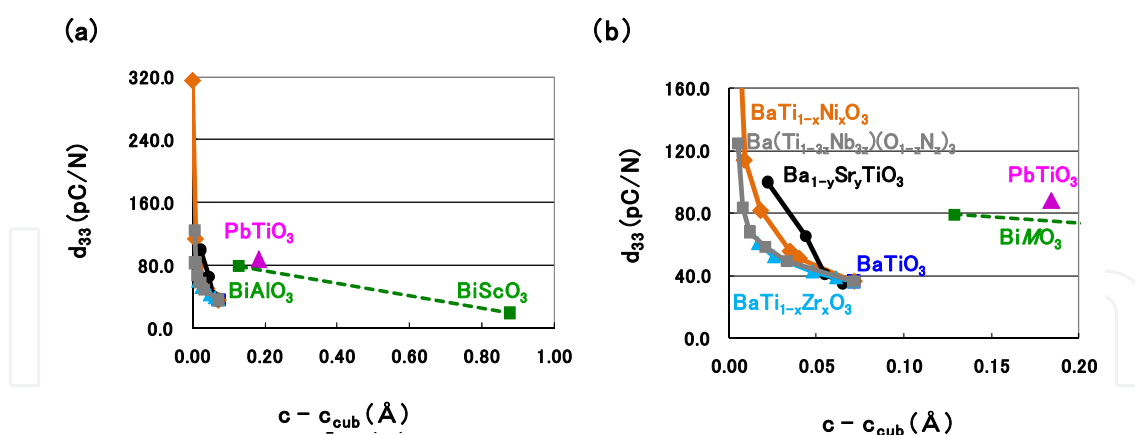


Figure 22. d_{33} as a function of $c - c_{cub}$ for different scales [15].

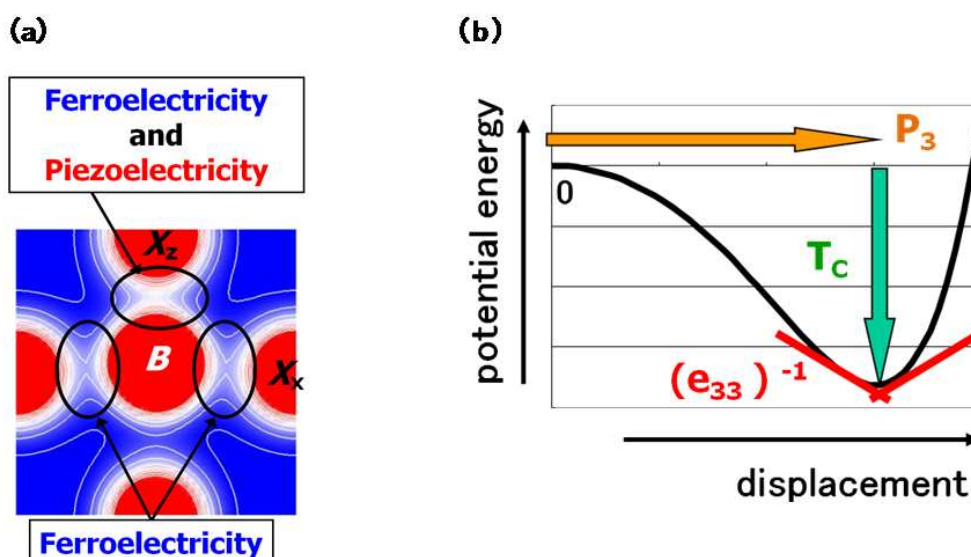


Figure 23. (a) Illustration of the relationship between the B-X Coulomb repulsions and the ferroelectric and piezoelectric states in tetragonal ABX_3 . (b) Illustration of the relationship between e_{33} and the deviation. P_3 and T_c denote the spontaneous polarization and the Curie temperature, respectively.

4. Conclusion

We have discussed a general role of the B-X Coulomb repulsions for ferroelectric and piezoelectric properties of tetragonal ABX_3 , based on our recent papers and patents. We have found that both ferroelectric state and piezoelectric state are closely related to the $B-X_z$ Coulomb repulsions as well as the $B-X_x$ ones, as illustrated in Fig. 23(a). Moreover, as illustrated in Fig. 23(b), we have also found that e_{33} is closely related to the deviation at the minimum point of the ΔE_{total} .

Acknowledgements

We thank Professor M. Azuma in Tokyo Institute of Technology for useful discussion. We also thank T. Furuta, M. Kubota, H. Yabuta, and T. Watanabe for useful discussion and computational support. The present work was partly supported by the Elements Science and Technology Project from the Ministry of Education, Culture, Sports, Science and Technology.

Author details

Kaoru Miura¹ and Hiroshi Funakubo²

¹ Canon Inc., Tokyo, Japan

² Tokyo Institute of Technology, Yokohama, Japan

References

- [1] Cohen R E. Origin of ferroelectricity in perovskite oxides. *Nature* 1992; 451 (6382) : 136-8.
- [2] Wu Z, Cohen R E. Pressure-induced anomalous phase transitions and colossal enhancement of piezoelectricity in PbTiO_3 . *Phys. Rev. Lett.* 2005; 95 (3): 037601, and related references therein.
- [3] Deguez O, Rabe K M, Vanderbilt D. First-principles study of epitaxial strain in perovskites. *Phys. Rev. B* 2005; 72 (14): 144101, and related references therein.
- [4] Qi T, Grinberg I, Rappe A M. First-principles investigation of the high tetragonal ferroelectric material $\text{BiZn}_{1/2}\text{Ti}_{1/2}\text{O}_3$. *Phys. Rev. B* 2010; 79 (13): 134113, and related references therein.
- [5] Wang H, Huang H, Lu W, Chan H L W, Wang B, Woo C H. Theoretical prediction on the structural, electronic, and polarization properties of tetragonal $\text{Bi}_2\text{ZnTiO}_6$. *J. Appl. Phys.* 2009; 105 (5): 053713.
- [6] Dai J Q, Fang Z. Structural, electronic, and polarization properties of $\text{Bi}_2\text{ZnTiO}_6$ supercell from first-principles. *J. Appl. Phys.* 2012; 111 (11): 114101.
- [7] Khenata R, Sahnoun M, Baltache H, Rerat M, Rashek A H, Illes N, Bouhafs B. First-principle calculations of structural, electronic and optical properties of BaTiO_3 and BaZrO_3 under hydrostatic pressure. *Solid State Commun.* 2005; 136 (2): 120-125.

- [8] Oguchi T, Ishii F, Uratani Y. New method for calculating physical properties from first principles-piezoelectric and multiferroics. *Butsuri* 2009; 64 (4): 270-6 [in Japanese].
- [9] Uratani Y, Shishidou T, Oguchi T. First-principles calculations of colossal piezoelectric response in thin film PbTiO₃. *Jpn. Soc. Appl. Phys.* 2008: conference proceedings, 27-30 March 2008, Funabashi, Japan [in Japanese].
- [10] Miura K, Kubota M, Azuma M, and Funakubo H. Electronic and structural properties of BiZn_{0.5}Ti_{0.5}O₃. *Jpn. J. Appl. Phys.* 2009; 48 (9): 09KF05.
- [11] Miura K, Furuta T, Funakubo H. Electronic and structural properties of BaTiO₃: A proposal about the role of Ti 3s and 3p states for ferroelectricity. *Solid State Commun.* 2010; 150 (3-4): 205-8.
- [12] Furuta T, Miura K. First-principles study of ferroelectric and piezoelectric properties of tetragonal SrTiO₃ and BaTiO₃ with in-plane compressive structures. *Solid State Commun.* 2010; 150 (47-48): 2350-3.
- [13] Miura K, Azuma M, Funakubo H. Electronic and structural properties of ABO₃: Role of the B-O Coulomb repulsions for ferroelectricity. *Materials* 2011; 4 (1): 260-73. <http://www.mdpi.com/1996-1944/4/1/260> (accessed 20 July 2012).
- [14] Miura K. First-principles study of ABO₃: Role of the B-O Coulomb repulsions for ferroelectricity and piezoelectricity. Lallart M. (ed.) *Ferroelectrics - Characterization and Modeling*. Rijeka: InTech; 2012. p395-410. Available from <http://www.intechopen.com/books/ferroelectrics-characterization-and-modeling/first-principles-study-of-abo3-role-of-the-b-o-coulomb-repulsions-for-ferroelectricity-and-piezoelec> (accessed 20 July 2012).
- [15] Miura K, Funakubo H. First-principles analysis of tetragonal ABO₃: Role of the B-O Coulomb repulsions for ferroelectricity and piezoelectricity. *Proceedings of 15th US-Japan Seminar on Dielectric and Piezoelectric Ceramics*, 6-9 November 2011, Kagoshima, Japan.
- [16] Miura K, Ifuku T, Kubota M, Hayashi J. Piezoelectric Material. Japan Patent 2011-001257 [in Japanese].
- [17] Miura K, Kubota M, Hayashi J, Watanabe T. Piezoelectric Material. submitted to Japan Patent [in Japanese].
- [18] Miura K, Furuta T. First-principles study of structural trend of BiMO₃ and BaMO₃: Relationship between tetragonal and rhombohedral structure and the tolerance factors. *Jpn. J. Appl. Phys.* 2010; 49 (3): 031501 (2010).
- [19] Miura K, Kubota M, Azuma M, and Funakubo H. Electronic, structural, and piezoelectric properties of BiFe_{1-x}Co_xO₃. *Jpn. J. Appl. Phys.* 2010; 49 (9): 09ME07.
- [20] Miura K, Tanaka M. Electronic structures of PbTiO₃: I. Covalent interaction between Ti and O ions. *Jpn. J. Appl. Phys.* 1998; 37 (12A): 6451-9.

- [21] LDA_TM_psp1_data: ABINIT. http://www.abinit.org/downloads/psp-links/lda_tm_psp1_data/ (accessed 20 July 2012).
- [22] Kuroiwa Y, Aoyagi S, Sawada A, Harada J, Nishibori E, Tanaka M, and Sakata M. Evidence for Pb-O covalency in tetragonal PbTiO₃. *Phys. Rev. Lett.* 2001; 87 (21): 217601.
- [23] Shannon R D. Revised effective ionic radii and systematic studies of interatomic distances in halides and chalcogenides. *Acta Crystallogr. Sect. A.* 1976; 32 (5): 751-67.
- [24] Suchomel M R, Fogg A M, Allix M, Niu H, Claridge J B, Rosseinsky M J. Bi₂ZnTiO₆: A lead-free closed-shell polar perovskite with a calculated ionic polarization of 150 μC cm⁻². *Chem. Mater.* 2006; 18 (21), 4987-9.
- [25] Khalyavin D D, Salak A N, Vyshatko N P, Lopes A B, Olekhnovich N M, Pushkarev A V, Maroz I I, Radyush T V. Crystal structure of metastable perovskite Bi(Mg_{1/2}Ti_{1/2})O₃: Bi-based structural analogue of antiferroelectric PbZrO₃. *Chem. Mater.* 2006; 18 (21), 5104-10.
- [26] Randall C A, Eitel R, Jones B, Shrout T R, Woodward D I, Reaney I M, Investigation of a high T_C piezoelectric system: (1-x)Bi(Mg_{1/2}Ti_{1/2})O₃-(x)PbTiO₃. *J. Appl. Phys.* 2004; 95 (7): 3633-9.
- [27] Rossetti Jr G A, Khachatryan A G. Concepts of morphotropism in ferroelectric solid solutions. Proceedings of 13th US-Japan Seminar on Dielectric and Piezoelectric Ceramics, 4-7 November 2007, Awaji, Japan, and related references therein.
- [28] Damjanovic D. A morphotropic phase boundary system based on polarization rotation and polarization extension. *Appl. Phys. Lett.* 2010; 97 (6): 062906, and related references therein.
- [29] Gonze X, Beuken J-M, Caracas R, Detraux F, Fuchs M, Rignanese G-M, Sindic L, Verstraete M, Zerah G, Jollet F, Torrent M, Roy A, Mikami M, Ghosez P, Raty J-Y, Allan D C. First-principles computation of material properties: the ABINIT software project. *Comput. Mater. Sci.* 2002; 25 (3), 478-92.
- [30] Hohenberg P, Kohn W. Inhomogeneous electron gas. *Phys. Rev.* 1964; 136 (3B): B864-71.
- [31] Opium - pseudopotential generation project. <http://opium.sourceforge.net/index.html> (accessed 20 July 2012).
- [32] Ramer N J, Rappe A M. Application of a new virtual crystal approach for the study of disordered perovskites. *J. Phys. Chem. Solids.* 2000; 61 (2): 315-20.
- [33] Resta R. Macroscopic polarization in crystalline dielectrics: the geometric phase approach. *Rev. Mod. Phys.* 1994; 66 (3): 899-915.
- [34] Kim Y-I, Lee E. Constant-wavelength neutron diffraction study of cubic perovskites BaTaO₂N and BaNbO₂N. *J. Ceram. Soc. Jpn.* 2011; 119 (5): 371-4.